Supplementary Information:

Attenuating Surface Plasmon Resonance via Core/Alloy Architectures

Peter N. Njoki, Louis Solomon, Wenjie Wu, Rabeka Alam, Mathew M. Maye*
Department of Chemistry, Syracuse University, Syracuse New York. U.S.A. mmmaye@syr.edu.

Experimental details:

Synthesis of Gold Nanoparticle Cores. Gold nanoparticles (Au, 13.6 ± 0.7 nm) were synthesized by a slightly modified citrate (Cit) reduction procedure. *(S1)* Briefly, a 1 mM $HAuCl_4$ solution was heated to ~95 °C for 30 minutes. To this solution a warm 38 mM trisodium citrate solution (10 mL) was added in one aliquot. Upon initial color change to red, the solution was then immediately cooled to ~80 °C and annealed for 1 hr. The sample was then let to cool naturally to room temperature and allowed to stir overnight. The solution was then stored protected from light. We found that the size of the Au increased with longer boiling times. The molar concentrations of gold nanoparticles ([Au]) were calculated via a measured extinction coefficient of 2.2×10^8 L $mole^{-1}$ cm^{-1}.

Layer-by-Layer Au_1Pd_{1-x} Alloy Shell Growth: To the Au cores synthesized above, alloy shells with sub nanometer thick layers (*n*) were deposited. The palladium ($[PdCl_4]^{2-}$) and gold $[AuCl_4]^-$) reduction is achieved using a minimum amount of reducing agent, sodium citrate (Cit), which was found only to reduce palladium and gold ions at the hydrothermal temperatures. Moreover, the precursor ions are added and reduced in a layer-by-layer fashion at a ratio (r =$[AuCl_4^-]$ + $[PdCl_4^{2-}]$/[Au]) required to deposit a 0.25~0.50 nm thick shell (t_S), based on model calculations for volume change and Au diameter and concentration. The alloy shell feed ratio was used to estimate alloy composition (x = $[AuCl_4^-]$ / $[AuCl_4^-]$ + $[PdCl_4^{2-}]$) in the text. Actual compositions were measured via XPS and EDX (see below).

In a typical experiment, a 2.2 mL ultrapure water (18.2 MΩ) solution of Au ([Au] = 9.3 nM), trisodium citrate ([Cit]=1.36 mM), $HAuCl_4$ ($[AuCl_4^-]$ = 0.045 mM)), and Na_2PdCl_4 ($[PdCl_4^{2-}]$ = 0.045mM are hermetically sealed in 10 mL glass microwave reaction vessels. Next, the sample is rapidly heated to hydrothermal temperatures (T_H) and pressures (P_H) using computer controlled microwave irradiation (MWI). A typical reaction time is 3 minutes. After each layer deposition (heating cycle), a 100 uL aliquot was collected for UV-vis and TEM analysis, and a fresh 100 uL aliquot of 1 mM $HAuCl_4$ and 1 mM Na_2PdCl_4 are added in different ratio while maintained the volume at 100 uL. The process is then repeated an *n* number of times, resulting in the growth of the Pd+Au-rich core/shell nanostructure (Au/Au_xPd_{1-x}). Between cycles, the Au/Au_xPd_{1-x} NPs were not purified. When heated at different temperatures for 3 min we observed a colorimetric change from the ruby-red color of the 14nm Au to a pinkish after only one layer (n=1), then gradually to purplish brown at n = 3-5. Ultimately, the color changed to (a) brownish at

increased shell thickness (*n*=10) for x = 0.25 and maroon for x = 0.75 at 120 °C. Similar results were obtained at 160 °C. The final Au/Au_xPd_{1-x} products were stored in the reaction mother liquor, and protected from light. Under these storage conditions, the Au/Au_xPd_{1-x} NPs were stable indefinitely.

Instrumentation:

*Synthetic Microwave Reactor***:** A Discovery-S (CEM Inc) synthetic microwave reactor was employed. The instrument is computer controlled, and operates at 0-300W, from 30-300 °C, and from 0-200 PSI. Temperature is monitored in-situ during synthesis via the use of an integrated IR-sensor, or via an immersed fiber optic temperature probe. The instrument is equipped with an active pressure monitoring system, which provides both pressure monitoring and added safety during synthesis. Pressure rated glass reaction vials with volumes of 10 or 35 mL were employed during synthesis. Active cooling was provided by the influx of the MW cavity with compressed N_2, which rapidly cools the sample at a controlled rate.

UV-visible Spectrophotometry (UV-vis): The UV-vis measurements were collected on a Varian Cary100 Bio UV-vis spectrophotometer between 200-900nm. The instrument is equipped with an 8-cell automated holder with high precision Peltier heating controller.

Transmission Electron Microscopy (TEM): TEM measurements were performed on a JEOL 2000EX instrument operated at 120 kV with a tungsten filament (SUNY-ESF, N.C. Brown Center for Ultrastructure Studies). Particle size was analyzed manually by modeling each particle as a sphere, with statistical analysis performed using ImageJ software on populations of at least 100 counts.

X-ray Photoelectron Spectroscopy (XPS): XPS analysis were performed at the Cornell Center for Materials Research (CCMR) on Surface Science Instruments (SSI) model SSX-100 that utilizes monochromated Aluminum K-α x-rays (1486.6 eV). The nanoparticles were drop cast onto a silicon wafer, and studied at an angle of 55^{o}, which corresponds to an analysis depth of ~5nm. The data was processed using CasaXPS software. Before analysis, each sample were purified free of any excess metallic ions by centrifugation.

High Resolution Transmission Electron Microscopy (HRTEM): HRTEM measurements were performed at the CCMR on a FEI T12 Spirit TEM/STEM operated at 120 kV with a field emission source

and a SIS Megaview III CCD camera. The instrument is equipped with both a brightfield and darkfield HAADF STEM detector. The selective area energy dispersive X-ray analysis (EDX) was performed in-situ to STEM visualization, using an EDAX Genesis X-ray detector with internal elemental calibration.

DDA Modeling: The NP and core/shell NP surface plasmon resonance (SPR) extinction spectra were modeled using the discrete dipole approximation (DDA) method developed by Draine and Flatau *(S2)*. The open source software package DDSCAT 7.07 *(S3)* was employed on a Linux workstation equipped with an Intel i7 processor and 12 GB SDRAM running Ubuntu. Isotropic cores were calculated via the ELLIPSOID DDSCAT routine, whereas core/shell morphologies were calculated via the CONELLIPS routine with defined core diameter, and shell thicknesses. Typical calculation times ranged from minutes for simple structures, to 12-24 hr for large diameters or complex core/shell geometries. In DDA (eq. 1) a numerical SPR solution is defined by dividing a NP into elemental cubic volumes that are characterized by their coordinates within the NP, and their subsequent polarizability *(S4)*. Thus, each unit can be treated as a dipole, the collection of which have shown great accuracy in describing not just SP λ_{max}, but also the entire shape of the SP band (i.e. accurate NP mapping):

$$\sigma_{ext} = \frac{4\pi k}{|\mathbf{E}_0|^2} \sum_{j=i}^{N} (\mathbf{E}^*_{loc,J} \bullet \mathbf{P}_J) \qquad (1)$$

Here, the SPR extinction ($\sigma_{ext,}$ Q_{ext}) is related to the sum of N discrete dipole vectors (fields) $\mathbf{E^*}$ and $\mathbf{P_J}$, corresponding to electrical field and polarization, and k is a constant ($k=m_0(2\pi/\lambda)$; m_0 = related to material index of refraction (eqn. 1). Wavelength dependent dielectric tables for both Au and Ag were generated using well-established optical constants *(S5)*. For the Au_XPd_{1-X} solid solution alloys, we calculated dielectric constants for a binary alloy by linear combination of individual Au and Pd values, namely: $\varepsilon_{Alloy}(x,\lambda)= x_{Pd}\varepsilon_{Pd}(\lambda)+(1-x_{Pd})\varepsilon_{Au}(\lambda)$; where x_{Pd} is the volume fraction of Pd, ε_{Au} and ε_{Pd} are the wavelength dependent dielectric constants for gold and palladium respectively. Such a method was recently described by El-Sayed and co-workers for Au and Ag system *(S6)*, and some theoretical work has been done recently *(S7)*. A similar approach was also used recently for alloy nanorods *(S8)*. The Au_xPd_{1-x} simulations were then employed for an alloy core, and core/alloy DDA calculations.

Supporting Figures:

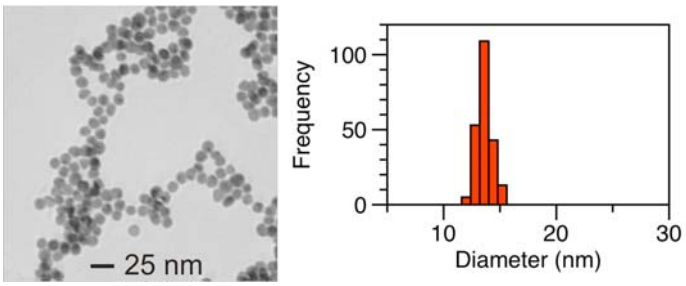

Figure S1: Representative TEM image and statistical analysis for Au seeds demonstrating a synthesized size of 13.6 ± 0.7 nm.

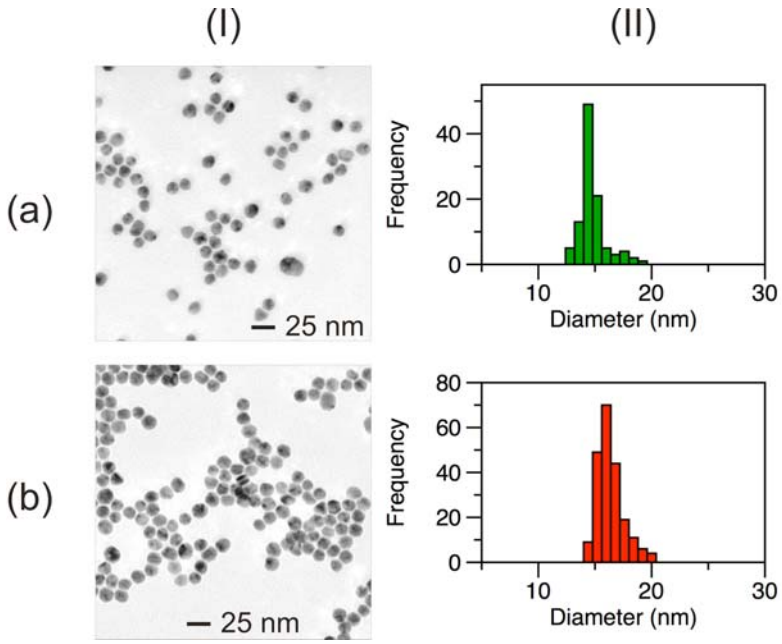

Figure S2: Morphological and optical comparisons for Au/Au_xPd_{1-x} prepared at T_H= 120 °C with x = 0.0. (I) TEM micrographs comparing shell layers *n* = 3 (a) and 7 (b) with (II) corresponding statistical analysis yielding 14.8 ± 1.2 nm and 16.4 ± 1.2 nm respectively.

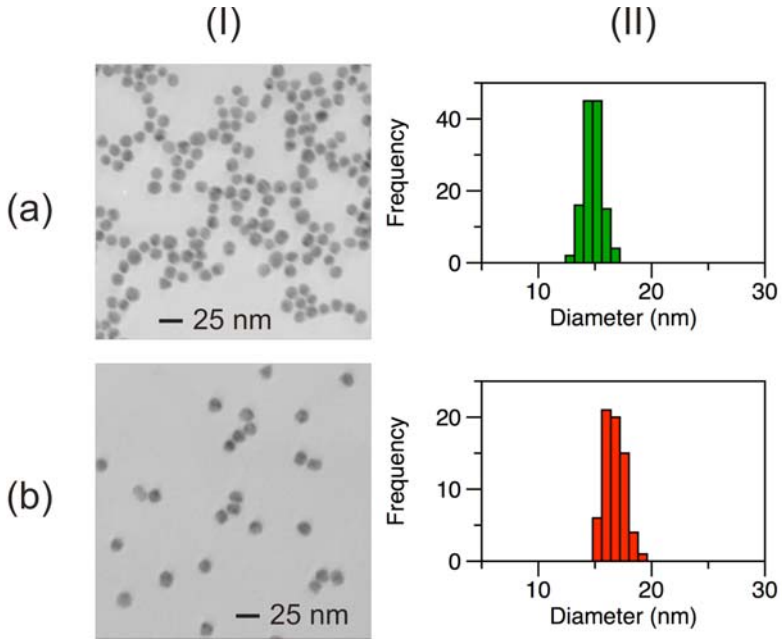

Figure S3: Morphological and optical comparisons for Au/Au_xPd_{1-x} prepared at T_H= 120 °C with x = 0.25. (I) TEM micrographs comparing shell layers *n* = 3 (a) and 7 (b) with (II) corresponding statistical analysis yielding 14.8 ± 0.7 nm and 16.7 ± 0.9 nm respectively.

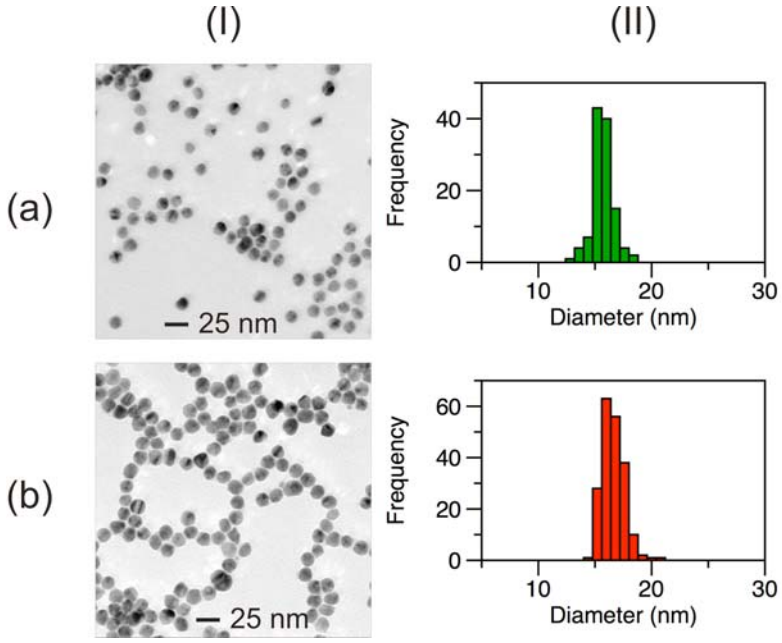

Figure S4: Morphological and optical comparisons for Au/Au_xPd_{1-x} prepared at T_H= 120 °C with x = 0.50. (I) TEM micrographs comparing shell layers *n* = 3 (a) and 7 (b) with (II) corresponding statistical analysis yielding 15.7 ± 0.9 nm and 16.6 ± 0.9 nm respectively.

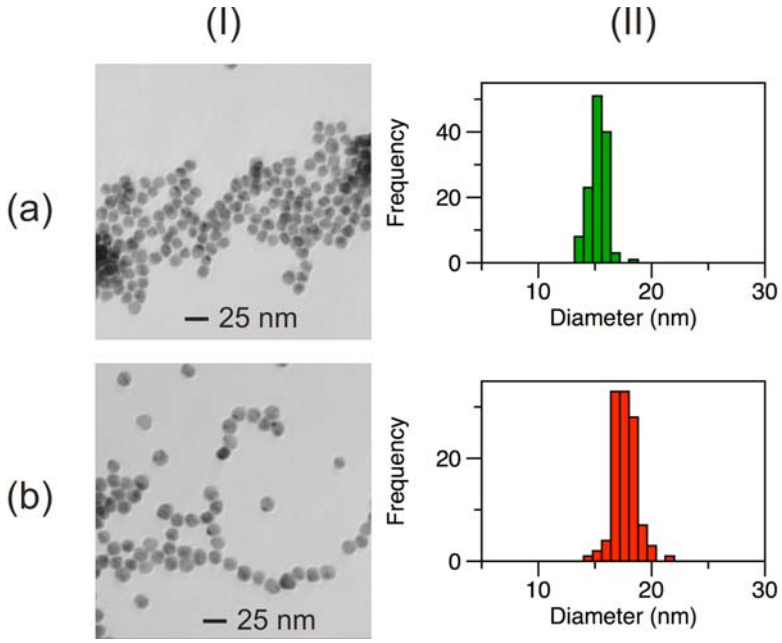

Figure S5: Morphological and optical comparisons for Au/Au_xPd_{1-x} prepared at T_H = 120 °C with x = 0.75. (I) TEM micrographs comparing shell layers *n* = 3 (a) and 7 (b) with (II) corresponding statistical analysis yielding 15.2 ± 0.7 nm and 17.6 ± 1.0 nm respectively.

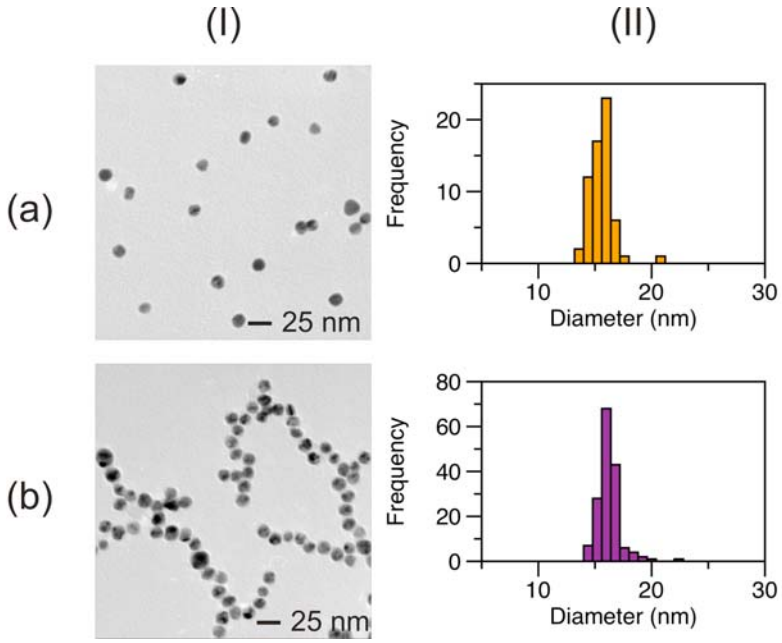

Figure S6: Morphological and optical comparisons for Au/Au_xPd_{1-x} prepared at T_H = 160 °C with x = 0.0. (I) TEM micrographs comparing shell layers *n* = 3 (a) and 7 (b) with (II) corresponding statistical analysis yielding 15.6 ± 1.1 nm and 16.3 ± 1.0 nm respectively.

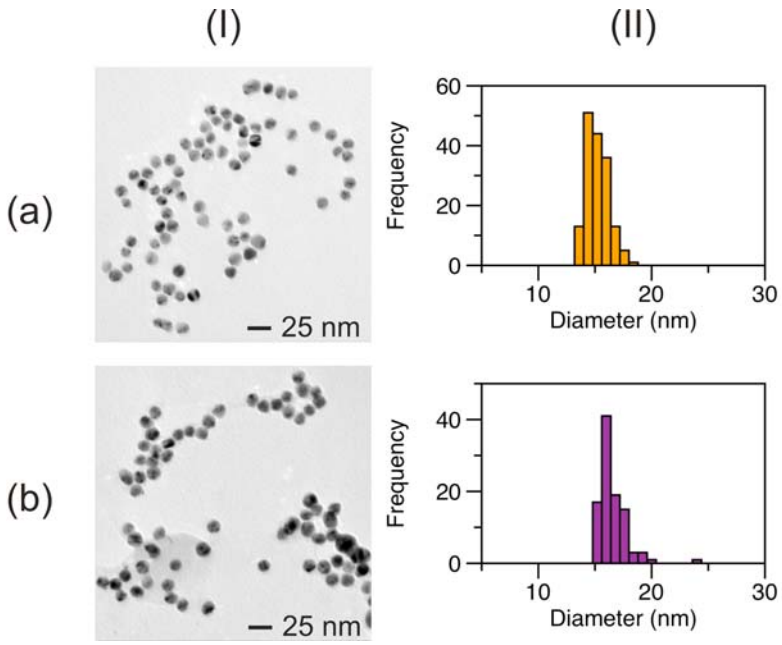

Figure S7: Morphological and optical comparisons for Au/Au_xPd_{1-x} prepared at T_H = 160 °C with x = 0.25. (I) TEM micrographs comparing shell layers *n* = 3 (a) and 7 (b) with (II) corresponding statistical analysis yielding 15.2 ± 0.9 nm and 16.6 ± 1.3 nm respectively.

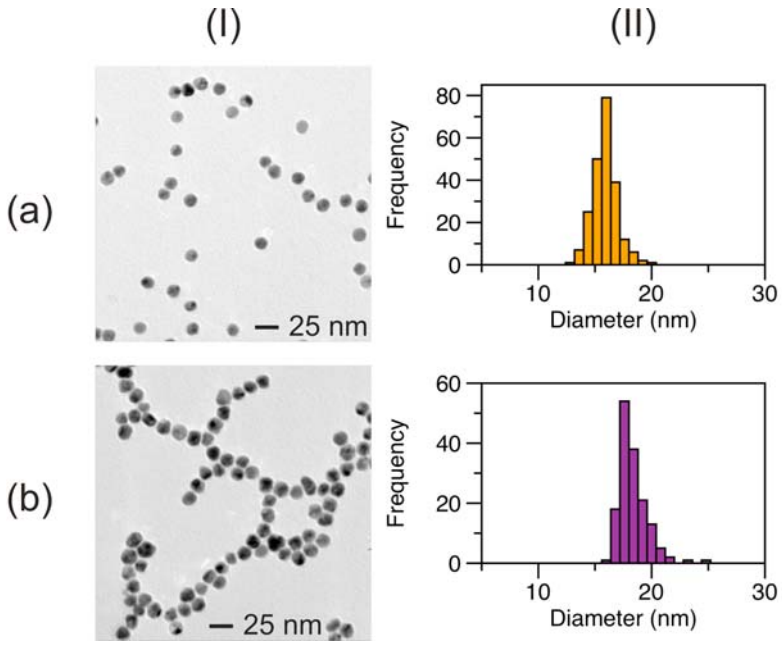

Figure S8: Morphological and optical comparisons for Au/Au_xPd_{1-x} prepared at T_H = 160 °C with x = 0.50. (I) TEM micrographs comparing shell layers *n* = 3 (a) and 7 (b) with (II) corresponding statistical analysis yielding 15.8 ± 1.1 nm and 18.4 ± 1.3 nm respectively.

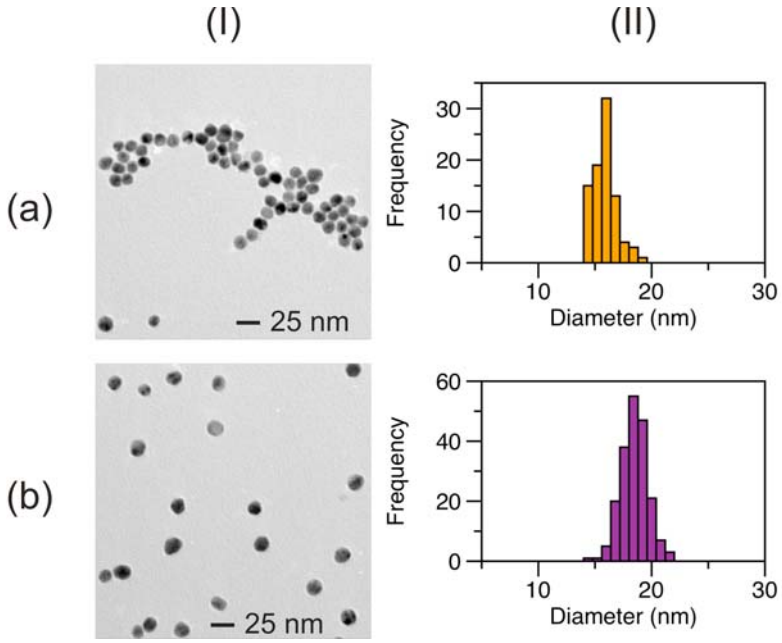

Figure S9: Morphological and optical comparisons for Au/Au_xPd_{1-x} prepared at T_H = 160 °C with x = 0.75. (I) TEM micrographs comparing shell layers *n* = 3 (a) and 7 (b) with (II) corresponding statistical analysis yielding 15.9 ± 1.1 nm and 18.4 ± 1.2 nm respectively.

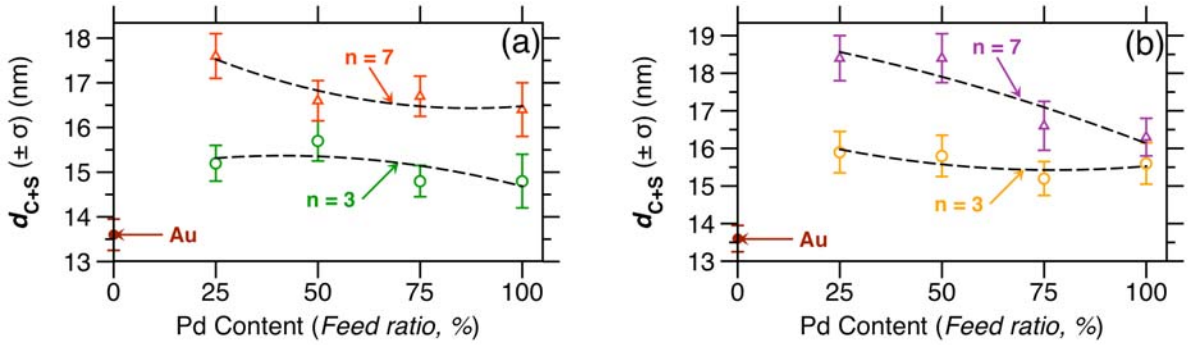

Figure S10: Comparison of d_{C+S} values after shell growth to *n* = 3 and 7 for T_H = 120 (a) and 160 °C (b).

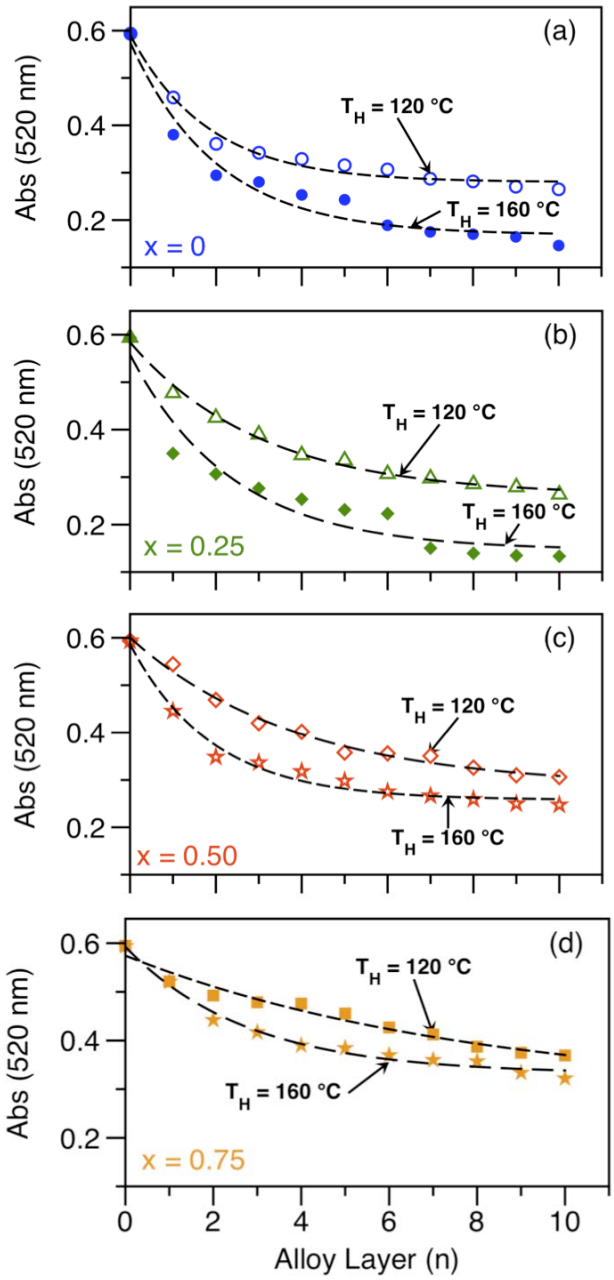

Figure S11: UV-vis extinction (λ_{SPR} = 520 nm) decrease as a function of Au_xPd_{1-x} deposition layer (*n*) at T_H = 120 °C and 160 °C for *x* = 0.00 (a), 0.25 (b), 0.50 (c), and 0.75 (d). Results indicate higher rate of SPR attenuation for higher *x*, and T_H = 160 °C.

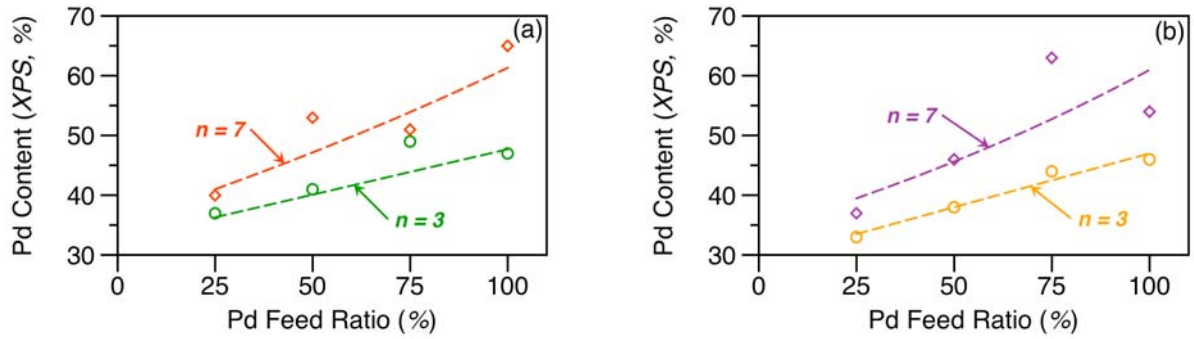

Figure S12: Results correlating alloy shell synthetic feed ratio with XPS determined NP composition for the Au/Au_xPd_{1-x} NPs prepared at T_H = 120 (a) and 160 °C (b) for layers n = 3 and 7.

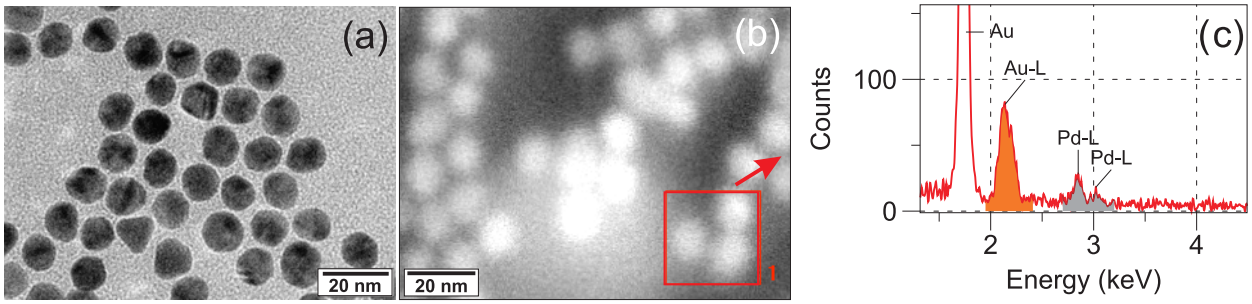

Figure S13: HRTEM (a), STEM (b), and EDX (c) results for Au/Au_xPd_{1-x} prepared at T_H = 160 °C, n = 7, and feed ratio x = 0.00. HRTEM and STEM images collected at different grid locations. Analysis of EDX collected at region shown in b results in overal NP composition of $Au_{77}Pd_{23}$. Analysis of multiple regions (not shown) resulted in an average composition of $Au_{73}Pd_{27}$.

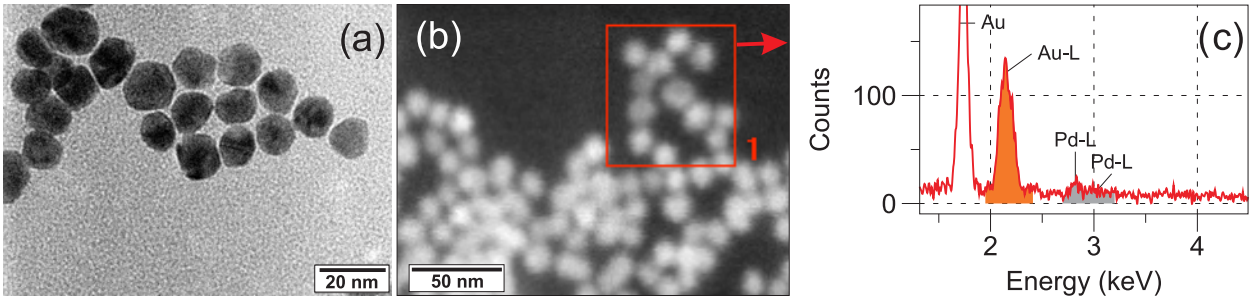

Figure S14: HRTEM (a), STEM (b), and EDX (c) results for Au/Au_xPd_{1-x} prepared at T_H = 160 °C, n = 7, and feed ratio x = 0.50. HRTEM and STEM images collected at different grid locations. Analysis of EDX collected at region shown in b results in overal NP composition of $Au_{96}Pd_4$. Analysis of multiple regions (not shown) resulted in an average composition of $Au_{89}Pd_{11}$.

Supporting References

S1 R. G. Freeman, M. B. Hommer, K. C. Grabar, M. A. Jackson, M. J. Natan, *J. Phys. Chem*. 1996, **100**, 718
S2 B. T. Draine and P. J. Flatau, *J. Opt. Soc. Am. A*, 1994, **11**, 1491-1499.
S3 B. T. Draine and P. J. Flatau, **2008**, "User Guide to the Discrete Dipole Approximation Code DDSCAT 7.0", http://arXiv.org/abs/0809.0337v5 (2008)
S4 B. T. Draine, P. J. Flatau, *J. Opt. Soc. Am. A* 2008, **25**, 2693-2703.
S5 P. B. Johnson, R. W. Christy, *Phys. Rev. B* 1972, **6,** 4370-4379.
S6 (a) S. Link, Z. L. Wang, M. A. El-Sayed, *J. Phys. Chem. B* 1999, **103**, 3529-3533. (b) K-S. Lee, M. A. El-Sayed, *J. Phys. Chem. B* 2005, **109**, 20331-20338. (c) S. Link, Z. L. Wang, M. A. El-Sayed, *J. Phys. Chem. B* 2006, **110**, 19220-19225.
S7 M. Moskovits, I. Srnova-Sloufova, B. Vlckova, *J. Chem. Phys.* 2002, **116**, 10435-10445.
S8 H-M Bok, K. L. Shuford, S. Kim, S. K. Kim, S. Park, 2009, **25**, 5266-5270.